International Journal of Multiphase Flow 120 (2019) 103088

Contents lists available at ScienceDirect

International Journal of Multiphase Flow

journal homepage: www.elsevier.com/locate/ijmulflow

A robust virtual-camera 3D shape reconstruction of deforming bubbles/droplets with additional physical constraints

Ashik Ullah Mohammad Masuk, Ashwanth Salibindla, Rui Ni*

Department of Mechanical Engineering, Johns Hopkins University, Baltimore, MD 21218, USA

ARTICLE INFO

Article history:
Received 17 June 2019
Revised 3 August 2019
Accepted 9 August 2019
Available online 17 August 2019

Keywords:
Bubbly flow
Non-affine deformation
3D shape reconstruction
Visual hull
Virtual camera

ABSTRACT

Bubbles and droplets in strong turbulence exhibit non-affine deformation, especially near a breakup event when the strong necking and interfacial instability begin to play roles. The virtual-camera (VC) method was designed and implemented to mitigate the limited-angle reconstruction problem for complex bubble/droplet geometries. The VC method incorporates the additional physical constraint of minimum surface curvature into reconstruction. This framework helps to reduce the reconstruction uncertainty for experiments studying multiphase flows that use a limited number of cameras, non-ideal camera positions, or the combination of both. The method was tested with three synthetic geometries– sphere, ellipsoid, and dumbbell–that represent the undeformed, gently-deformed, and severely-deformed bubbles. In addition, a DNS dataset of bubbles with a 2% void fraction in turbulent channel flow was also utilized to generate a synthetic dataset for tests, and the volume overestimation was found to decrease from over 20% to about 10% after implementing the VC method. Finally, the method was applied to the experimental dataset of bubble-turbulence interaction, and the result shows over 20% improvement in volume estimation. An indirect uncertainty quantification that relies on the bubble aspect ratio and orientation has also been developed to estimate the bubble reconstruction uncertainty in each frame. This allows a more selective postprocessing step to obtain the statistics of deformation and breakup based on the quality of reconstruction.

1. Introduction

Multiphase flows are more common than their single-phase counterpart in many natural and industrial applications, such as solid particles in dust storms (White, 1982), bubble-mediated gas transfer in the ocean (Woolf, 1997), two-phase heat transfer in energy systems (Sun et al., 2002), and fermentation in biochemical reactors (Galindo et al., 2000). Out of all types of multiphase flows, flow that consists of only two phases is the simplest and may serve as a canonical case for understanding the complex interfacial mass, momentum, and energy transfer between two phases.

In gas-liquid or liquid-liquid two-phase flows, bubbles and droplets may behave either as rigid or deformable objects depending on their sizes, inner viscosity, density difference, and surface tension. For some cases, deformation is driven completely by buoyancy, in which the deformation is simple and can be reconstructed with only two cameras. For many other instances, bubbles subjected to strong turbulence may experience extreme stretching and distortion, leading to complicated non-affine deformation. This type of deformation dynamics must be revealed by a robust shape reconstruction method that can deal with complex geometries.

One method that has been attempted is to reconstruct the bubble geometry by fitting an ellipse to the projected outline on each camera (Ravelet et al., 2011; Jordt et al., 2015; Besagni and Inzoli, 2016; Giovannettone et al., 2009; Maldonado et al., 2013), and these ellipses were combined in 3D to get the final ellipsoid. This step tends to remove some key deformation features. The underlying assumption used in the reconstruction is that the bubble deformation is always affine with no bending, surface wave, or any high-order deformation, even though some of these dynamics could be very important in turbulent multiphase flow.

To improve this method, a slicing technique has been proposed and used by many groups (Fujiwara et al., 2004; Honkanen, 2009; Fu and Liu, 2018). This technique refines the entire geometry by smoothing each horizontal slice by fitting it either with an ellipse (Fujiwara et al., 2004; Honkanen, 2009) or a spline (Fu and Liu, 2018). Selecting the Note that the slicing method was designed primarily for studying bubble rising in a quiescent medium, where the bubble deformation is driven by the buoyancy. If the deformation is chaotic and strongly non-affine, this method may not work

* Corresponding author.
E-mail address: rui.ni@jhu.edu (R. Ni).

https://doi.org/10.1016/j.ijmultiphaseflow.2019.103088
0301-9322/

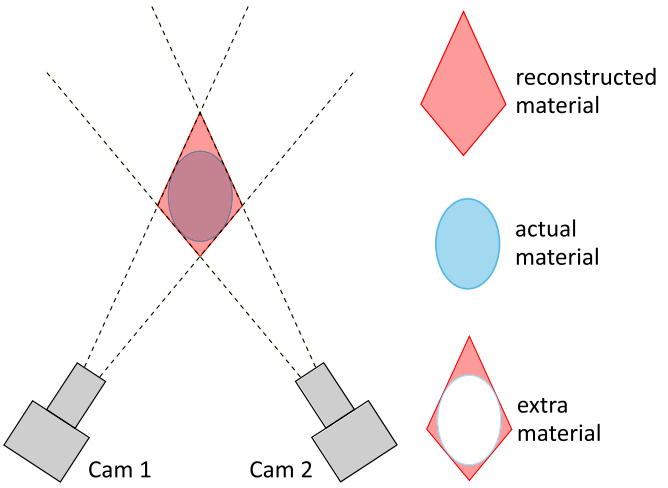

Fig. 1. Schematic of the limited-angle VH Reconstruction, which tends to result in an overestimation of the volume.

so well since it may become necessary to also slice and smooth in other directions. But along which direction to slice is the question.

To broaden the scope of the discussion, it is worth noting that reconstructing a complex geometry is also prevalent in computer vision for different applications. In particular, silhouette-based (also known as the visual hull technique) method has been used extensively (Mulayim et al., 2003; Matusik et al., 2000; Laurentini, 1994; Kutulakos and Seitz, 2000). In this method, sihouettes of an object are projected onto cameras that focus on the same view volume from different angles. To obtain the 3D reconstructed volume of an object, as shown in Fig. 1 (top view), cone-like volumes are extruded from 2D images, and the intersection of these cones from different cameras forms the visual hull (VH) of the object. This technique has also been used in medical instruments such as computerized tomography (CT) (Sidky and Pan, 2008). In order to provide an accurate shape reconstruction, a typical VH method requires using either many cameras or rotating one camera to cover as many angular views as possible (Medoff et al., 1983; Sidky et al., 2006).

For turbulent multiphase flow, the typical timescale is in milliseconds. The complex dynamics of deformation has to be recorded using high-speed cameras. The price of high-speed camera is often so high that two to four already reach the limit of the budget for many experiments. For turbulent multiphase flow, neither many cameras nor many angles are viable options. In this scenario, the problem becomes the limited-angle or limited-data reconstruction, in which case the number of constraints is limited and the problem becomes underdetermined. As a result, the limited-angle VH reconstruction is associated with extra materials that come from the volume shadowed by the object itself, as shown in Fig. 1. Nevertheless, the VH method has been used to study many multiphase flow phenomenon e.g., boiling (Rau et al., 2016), rising bubbles (Fu and Liu, 2018), and complex-shape rigid objects (Adhikari and Longmire, 2012).

The VH method can be improved if some *a priori* knowledge of an object is available. For example, the shape of a moving insect can be reconstructed based on the known anatomical structure of its body (Ristroph et al., 2009). The surface texture and color of objects have also been used to improve the reconstruction (Isidoro and Sclaroff, 2003; Furukawa and Ponce, 2009; Kanatani and Chou, 1989). In the context of turbulent multiphase flows with bubbles and droplets, most of these methods to improve VH cannot be implemented directly due to bubbles' high deformability, transparency, interface reflection, and the absence of colored textures.

Bubbles and droplets have their own unique physical constraint, surface tension. Even under extreme stretching, the surface tension still attempts to minimize the surface area and decrease the surface curvature. In contrast, most extra materials produced by the limited-angle VH method tend to have sharp corners because of the intersection of two lines-of-sight, as shown in Fig. 1. Implementing this physical constraint into the reconstruction is nevertheless nontrivial. Medoff et al. (1983) and references within presented a general framework to incorporate all available *a priori* information using the iterative convolution backprojection algorithm. Although this technique is designed for X-ray CT data that deals with streak artifacts that are not relevant to our optical system, this idea can still be applied to our case to account for the surface tension constraint.

In this article, a simple algorithm to improve the 3D reconstruction of deformable bubbles in turbulent flow will be introduced. The idea of this method is to spread the minimum interfacial-area constraint to many view angles that are not covered by real cameras, hence the name "virtual camera". The method will be tested on (i) three synthetic geometries with different aspect ratios and orientations, (ii) a DNS dataset of turbulent channel flow, and (iii) our experimental dataset in fully-developed turbulence. In addition, we will introduce a novel way to independently assess the reconstruction uncertainty of the experimental data by using the aspect ratio and orientation information. This allows us to be more selective in the postprocessing step.

2. Volume of reconstruction

2.1. Challenges and solutions

As shown in Fig. 1, for the limited-angle VH reconstruction, there are some important features of the excess materials: (a) As shown in Fig. 1, the extra materials are shadowed by the object itself and hidden within a volume bounded by the intersection of lines of sight from cameras. (b) The volume of the extra materials drops as the number of real cameras increases. Depending on the geometrical complexity of the object of interest, there is a limit in terms of the number of cameras needed, above which the benefit of adding one extra camera is outweighed by the cost and complexity of the setup. (c) The most efficient way to remove the extra material is to position another camera from a direction that clearly views the shadowed extra material. One example is shown in Fig. 1. If the optical axes of two cameras lie on a plane, the optimal orientation of the third camera should be perpendicular to that plane.

For 3D fluid dynamics measurements, it is a standard to position four cameras on one side facing towards the view volume with small angles among them. There are two reasons for this camera configuration: (i) flow and laser typically take two orthogonal directions, which leave only one direction for cameras. (ii) For 3D Tomographic particle image velocimetry (Tomo-PIV) or particle tracking velocimetry (PTV), the only information that is needed for a particle is its center of mass, which only has three degrees of freedom. The angle separation among four cameras, albeit small, is sufficient to extract the particle motion (Ouellette et al., 2006; Ni et al., 2012). If particles have finite size and are deformable, the degrees of freedom grow significantly, and one would need much larger angle separation among cameras to resolve the complicated deformation.

In Fig. 2, a simple finite-size sphere is reconstructed using a 4-real-camera configuration typically used in 3D Tomo-PIV. The reconstructed volume (gray) using the standard VH method has a spindle shape with two tips pointing in the direction towards four cameras. The excess material hidden in these two tips represents a volume that is shadowed by the sphere itself. This extra volume

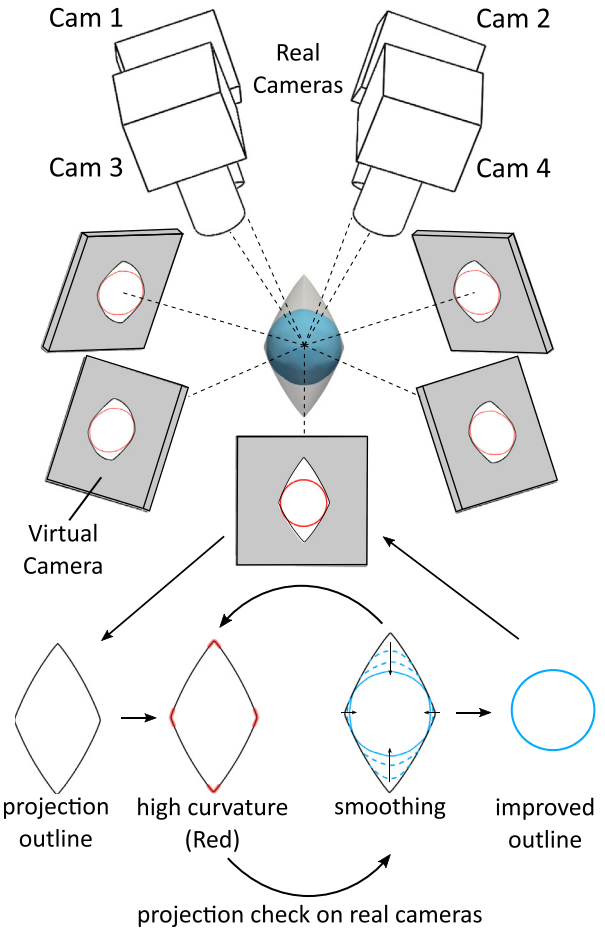

Fig. 2. Schematic of the classical VH and our VC method with four-real-camera configuration (top). Gray panels indicate the virtual cameras. On each panel, the black outline marks the reprojection from the VH reconstructed geometry, and the red outline marks the smoothed ones after several iterations (bottom) that can be used to obtain the blue sphere.

constitutes about 30% of the actual sphere volume and leads to an overestimation of the aspect ratio by a factor of 2.

2.2. Virtual camera method

To address the problem experienced in the limited-angle VH reconstruction, the VC method is designed and implemented. The method incorporates an *a priori* physical constraint, the minimal surface area, in virtual cameras that are positioned along directions that are not accessible by real cameras.

The steps involved in the VC method are illustrated in Fig. 2 and discussed in details as follows:

Step 1: The first step is to process images acquired from real cameras to separate bubbles from the background. These processed images are then fed to the classical VH method to determine the first initial 3D reconstruction of all bubbles in the field of view. As shown in Fig. 2, for four real cameras closely packed along the vertical direction, the initial reconstruction of a sphere looks like a spindle with two pointing tips, as shown by the gray volume in the center.

Step 2: Virtual cameras need to be positioned along the directions that are least covered by all the existing cameras. In practice, a code was designed to achieve this by minimizing the objective function $Z = \max(\theta_i)$, where θ_i represents the obtuse angle between the newly-added virtual camera and the i_{th} existing one, both real and virtual. Following this method, the first virtual camera, in the case shown in Fig. 2, should be positioned facing towards the reader. The initial reconstructed volume is then projected to this view. The outline of the projected shape clearly shows the two pointing tips.

Step 3: An iterative process then starts in order to remove the sharp corners of the projected outline without affecting bubble images on real cameras. This process is illustrated at the bottom of Fig. 2 and will be briefly introduced here.

(a) 2D curvature along the entire projected outline is determined.
(b) Locations with high curvature are identified. The outline near the high-curvature corner is smoothed by averaging the points in the vicinity. The difference between the areas covered by the smoothed and original outlines is A_{virt}.
(c) The smoothed outline from this virtual camera is added to the reconstruction along with other cameras, and a new 3D volume is generated by using the VH method.
(d) The newly-reconstructed volume is then projected onto all real cameras. If the projected area differs from the actual area by less than 10% of A_{virt}, the smoothing procedure is accepted and the iteration continues. Otherwise, the reconstruction is reverted to the previous iteration, and the entire iteration stops.

This method allows us to remove most reconstruction artifacts with minimum impact on the actual volume. However, this is the most time-consuming step that can be accelerated by GPU or high-performance computing clusters in the future.

Step 4: Virtual cameras are added one by one, and step 2 to 3 are repeated until adding one more virtual camera does not provide significant benefit. For our experiments, in most cases, 17 virtual cameras are sufficient.

For a convex geometry, this method works for as few as two real cameras. In Fig. 3, a sphere was reconstructed using (a) two real cameras and (b) three real cameras. In both cases, cameras are placed orthogonal to each other. If only the VH method is applied, the extra material, indicated by the gray volume, reduces from 31% to 15% as N_{cam} increases from 2 to 3. On the other hand, the volume uncertainty drops below 3% for both 2 and 3 real cameras after implementing VC. This indicates that the VC method works well for even just two real cameras as long as the geometry is simple and convex. Relatively more benefit is gained from the VC method for two real cameras than that for three real cameras.

3. Experimental apparatus

Fig. 4(a) shows the experimental setup. Six high-speed cameras were used to cover the perimeter of the test section of a vertical water tunnel (V-ONSET). The azimuthal angles of all cameras are shown in the top view (Fig. 4(b)), and their individual inclination angles are indicated on the side. For the rest of the paper, all analyses of the synthetic datasets were performed based on this camera configuration. Although the exact uncertainty varies with the camera configurations chosen, the overall principle can still be learned from this example.

The water tunnel used in our experiment is aligned vertically, allowing its mean flow to balance the rising velocity of buoyant bubbles. This flow configuration forbids the optical access into the test section from the top or bottom as these directions are occupied by the mean flow. To mitigate this problem, three cameras (Cam 3, Cam 5, and Cam 6) were tilted away from the horizontal plane to acquire information from the third axis. No prism was used for inclined cameras. For these cameras, 22° is probably the

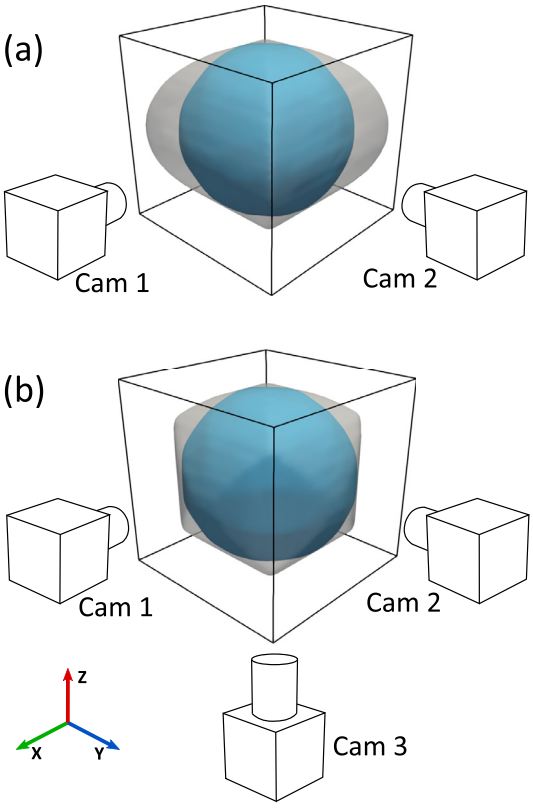

Fig. 3. Schematic of the 3D reconstruction of a sphere with (a) two real cameras and (b) three real cameras. Gray color represents the geometry reconstructed by the limited-angle VH method, and the blue color represents the geometry reconstructed by the VC method.

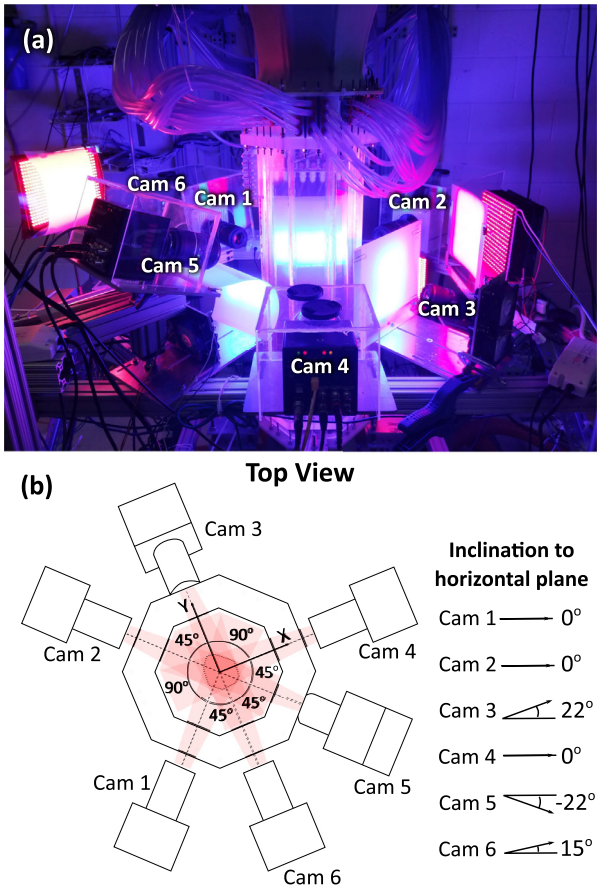

Fig. 4. (a) Photo of the vertical tunnel V-ONSET with six cameras and their LEDs; (b) Top view of the camera configuration with respect to the octagonal test section; the inclination angle of each camera from the horizontal plane is also marked.

largest inclination angle that one can use and still be able to reach a similar calibration accuracy in our facility without a prism. For each camera, a dedicated high-power LED array was used to illuminate bubbles.

3.1. Calibration

Six cameras have to be carefully calibrated to establish a correspondence between points in space and points on images (Tan et al., 2019). Such a relationship is acquired by imaging a pattern on a calibration target by all the cameras simultaneously. In our setup, since cameras cover the entire perimeter of the test section, some cameras have to view the target from behind. A transparent acrylic target with a known thickness and refractive index was used. One side of the target was laser-etched with some dots. These dots can be viewed from both sides. For cameras viewing the dots from behind through a layer of acrylic, the calibration parameters have to be corrected to account for the refractive-index difference between acrylic and water. After the correction, the final nominal calibration uncertainty is about 0.5 pixels.

The initial calibration uses the classical Tsai's model (Tsai, 1986) to recover the camera transfer function in terms of the interior parameters and exterior parameters. The exterior parameters connect a 3D scene in the physical space to the camera coordinates. The interior parameters link the 3D points to its corresponding 2D locations. Additional radial and linear distortion coefficients were also calibrated.

After the initial calibration, tracer particles of 50 μm in diameter were injected into the view volume; the number of particles in the view was kept very low (~100 particles) to ensure that the inter-particle distance is large enough to avoid ambiguity. Water was stirred gently to move these particles, and their positions were triangulated and tracked using our in-house particle tracking code with the initial calibration configuration. The search radius that was used to triangulate particles was set at 0.2 mm to find all possible candidates. Only the tracked particles exceeding 100 frames were selected. Their positions were distributed over the entire view volume, but not uniformly. To avoid possible risks of calibration bias, certain sub-volumes that had more particles than others were randomly down-sampled to ensure a similar number density of particles throughout the entire volume. Finally, these particles and their corresponding images were used to conduct a non-linear optimization to find an optimal set of camera parameters that would minimize the intersection errors of all epipolar lines, the so-called self calibration method. The uncertainty error was reduced from 0.5 to 0.2 pixels after this step.

The importance of this step has been widely accepted in the Tomo-PIV (Wieneke, 2008). Comparatively less attention has been paid to bubble shape reconstruction, partly because the requirement of accuracy is different. In PIV, particle size is only two to three pixels in diameter, and tracking them requires an accurate determination of their center to the sub-pixel level. Bubbles are much larger so calibration was conducted typically without the volumetric self-calibration. Nevertheless, it was emphasized before by Wieneke (2008) that, without this step, one is not even aware of how large the calibration errors actually are.

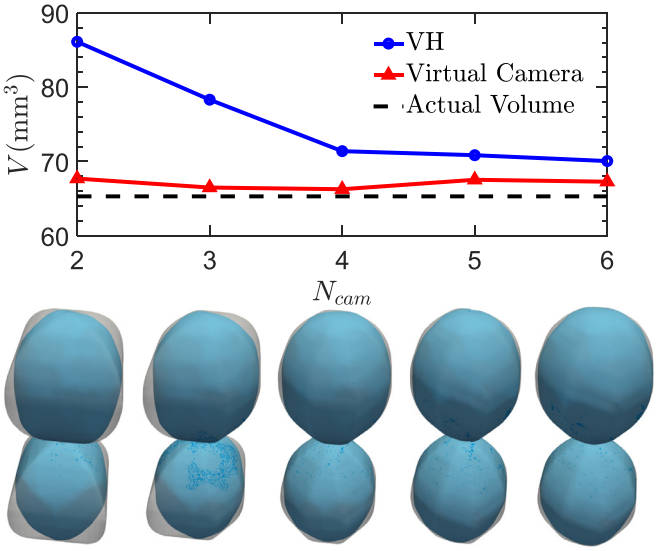

Fig. 5. The reconstructed volume V of a synthetic dumbbell versus the number of real cameras N_{cam}. Five 3D objects indicate the reconstructed geometry for N_{cam} from 2 to 6. For each object, the gray color represents the VH-reconstructed volume, whreas the blue color indicates the VC-reconstructed results.

4. Results

When a bubble starts to deform and its shape deviates away from a perfect sphere, the reconstruction becomes sensitive to the nature of the shape, e.g., concave or convex, which can be represented by a dumbbell or an ellipsoid, respectively. These two geometries are representative of either the weakly-deformed or severely-deformed states. All tests introduced in the rest of this paper use the camera configuration adopted in our experiments. For tests that use fewer than six cameras, some real cameras were removed.

Fig. 5 shows a dumbbell oriented vertically and visualized by two to six real cameras. This dumbbell geometry is generated by using the spherical harmonics $Y_m^l(\theta,\phi)$, with degree $l=1$ and order $m=0$. This particular orientation allows all real cameras to see the neck of this dumbbell. The blue line shows the reconstructed volume V as a function of the number of real cameras N_{cam} used in the standard VH reconstruction. As N_{cam} increases, V approaches the actual volume (dashed line) as expected. The volume drops quickly for $N_{cam}<4$, suggesting that one would ideally need four cameras for this complex shape if only VH is applied. The reconstructed volume using the VC method is shown as the red curve, which almost overlaps with the dashed line, indicating that the reconstruction is very accurate and insensitive to N_{cam}. The comparison of the reconstructed geometry between VH and VC is shown as the gray and blue 3D geometries in the lower panel of the figure. As one can see, the method successfully removed the extra materials, especially for small N_{cam}.

The reconstruction uncertainty is also sensitive to the orientation of the object, which can be represented by the Euler angles (ϕ, θ, ψ). The Euler angle at (0°, 0°, 0°) is shown in Fig. 6(a). For this orientation, the major axis of the dumbbell aligns with the vertical axis. Since the generated dumbbell is symmetrical about the major axis, just θ and ϕ are sufficient to represent all the orientations.

In Fig. 6(b), the volume reconstruction uncertainty ϵ_V is shown as a function of θ and ϕ. When all six cameras view the neck at $\theta=0°$ (Fig. 6(a)), the uncertainty is the smallest at around 5%. When the dumbbell lies down and its major axis falls on the horizontal plane at $\theta=90°$, the view of its neck for several cameras can be shadowed by its two large ends. For this orientation, the uncertainty really depends on how many real cameras can see the neck. At $\phi=60°$, three cameras still have rather clear views, resulting in 23% uncertainty. As shown in Fig. 6(c), the worst case occurs at $\phi=0°$, where the uncertainty is 28%. In this case, the dumbbell is almost pointing towards three cameras, completely blocking their views. As the result, the reconstructed volume has significant amount of excess materials at the neck. After implementing the VC method, it can be seen that all the uncertainties systematically reduce. At $\theta=90°$, ϵ_V decreases by nearly 10%. However, the remaining extra material is still about 20% because the algorithm cannot refine the neck that cannot be seen.

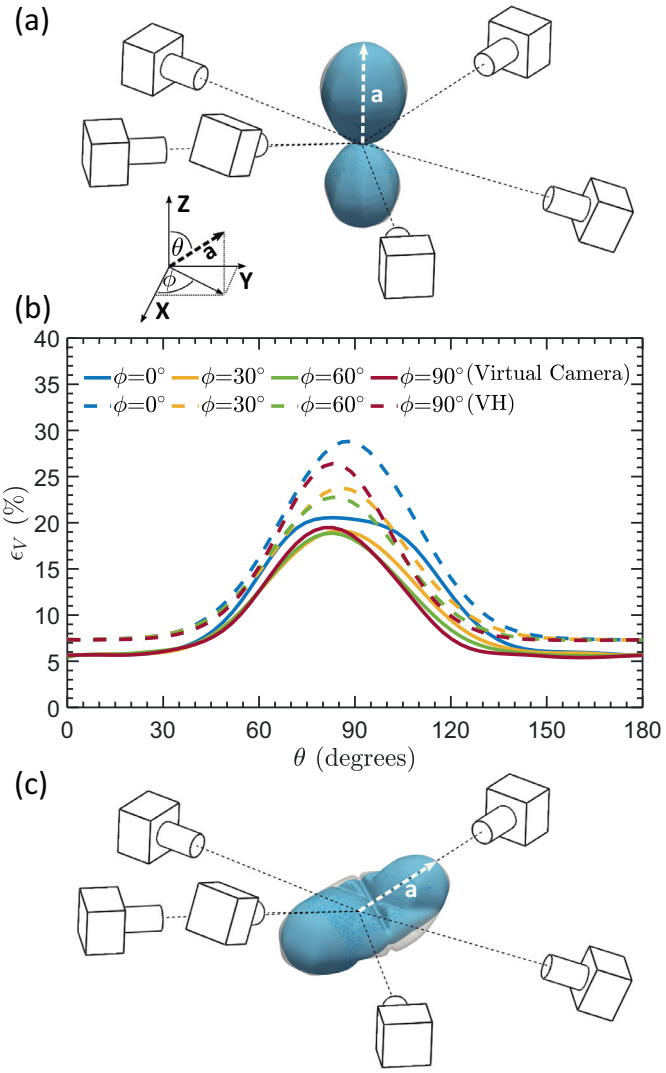

Fig. 6. (a) A dumbbell with its Euler angle at (0°, 0°, 0°) surrounded by six real cameras. (b) The volume reconstruction uncertainty ϵ_V versus two Euler angles θ and ϕ. Dashed lines and solid lines are for the VH and VC method, respectively. (c) The reconstructed dumbbell geometry with extra mass at the neck when the Euler angle is at (0°, 90°, 0°).

A dumbbell represents a bubble that is close to breakup, which is an extreme case with a large uncertainty. Most deforming bubbles are probably closer to ellipsoids until the moment of breakup. A similar test has also been performed with a synthetic ellipsoid with the major and two minor axes of 4.5 mm, 2.5 mm, and 1.5 mm in length, respectively. The volume uncertainty ϵ_V is shown as a function of θ and ϕ in Fig. 7(a). ϵ_V appears to be low $<10\%$ for all orientations and does not show strong dependence on either angle. In particular, at $\theta=90°$, the peak ϵ_V is about 11%, which is

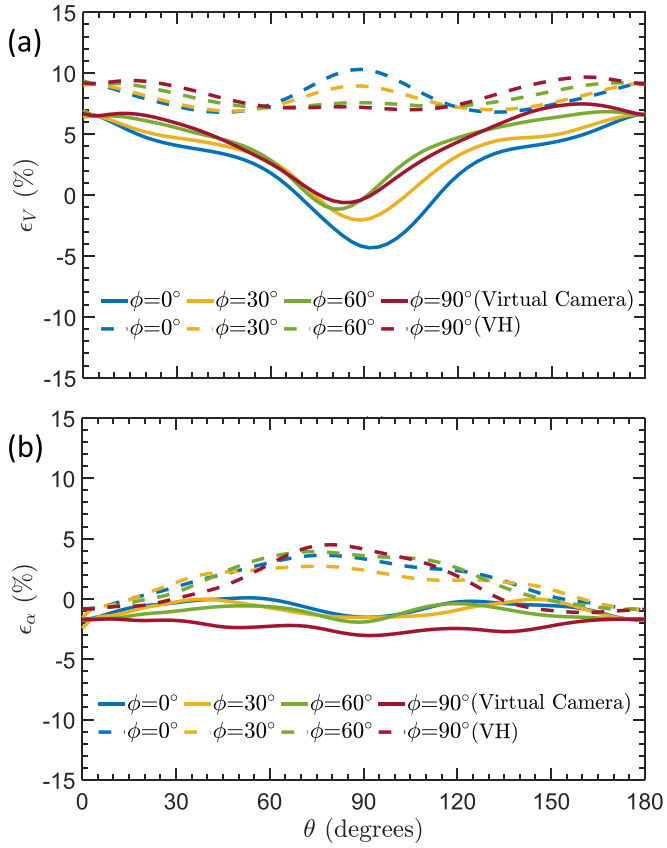

Fig. 7. The reconstruction uncertainty of (a) volume ϵ_V and (b) aspect ratio ϵ_α of an ellipsoid as functions of its two Euler angles θ and ψ.

much smaller than that of the dumbell $\epsilon_V = 28\%$. After using the VC method, ϵ_V reduces to $\sim \pm 5\%$.

In addition to ϵ_V, the aspect ratio uncertainty ϵ_α is also sensitive to the reconstruction accuracy. As shown in Fig. 7(b), the classical VH method systematically overestimates α, and the peak value of ϵ_α is about 5% at $\theta = 90^\circ$. After implementing our VC method, ϵ_α becomes very close to zero for all orientations.

5. Synthetic test case using a DNS dataset

Although sphere, ellipsoid, and dumbbell respectively represent the undeformed, weakly-deformed, and severely-deformed geometry of a bubble, they do not reflect the non-affine deformation that bubbles tend to experience in turbulence. A DNS dataset of bubbles in turbulent channel flow was utilized to generate a synthetic test case to evaluate the code performance of handling the non-affine deformation (Lu and Tryggvason, 2008). Only one randomly-picked snapshot was used as the test case. As shown in Fig. 8(a), there are 19 bubbles within this frame, and they are representative of the realistic bubble deformation in turbulence. Most of these bubbles cannot be modeled as simple ellipsoids.

The synthetic images, cropped only to the part with bubbles, on all six real cameras are shown in Fig. 8(a). Only about 1/4 of the total camera resolution was used, and the full camera image could cover as many as 80 bubbles. In each camera, at least two pairs of bubble images appear to be overlapped because the void fraction for this particular dataset is about 2%, which is relatively high for the 3D optical reconstruction.

During the reconstruction, we realize that overlapping bubbles can be automatically segmented as long as at least one camera can view them as two separate bubbles. It is, in fact, safer to allow the reconstruction method to separate bubbles than attempting segmentation in 2D (Fu and Liu, 2016) for all cameras, as a highly-deformed bubble can be easily mistreated as two overlapping bubbles. For our experiments, using six real cameras would also help to maximize the possibility of having at least one camera viewing the gap between two separate bubbles.

In Fig. 8(a), although there are about two to five pairs of bubbles overlapping with each other in each camera. fortunately, most overlapping images do not appear on more than two cameras for the same pair of bubbles, which leaves with more than four

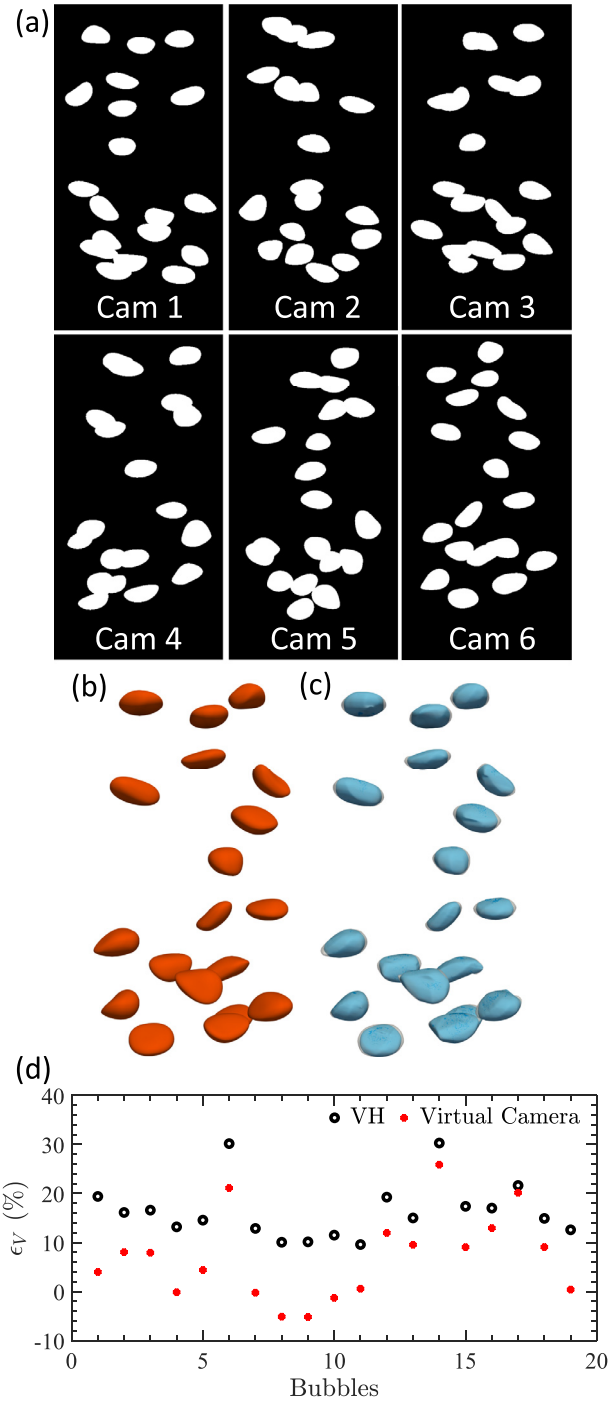

Fig. 8. (a) Synthetic images of a DNS bubble data on all six real cameras; (b) The geometry of 19 bubbles from the DNS data; (c) The reconstructed geometry (gray, VH; blue, virtual camera); (d) The volume reconstruction uncertainty ϵ_V for all 19 cases with black circles for VH and red dots for the VC method.

cameras to reconstruct the bubble geometry. This explains why the reconstruction results in Fig. 8(c) has no discernible difference from the simulation result shown in Fig. 8(b).

Fig. 8(d) shows ϵ_V for all the bubbles in the frame. For most cases, after implementing our VC method, ϵ_V reduces to $\pm$ 10%, which suggests that our method works well even for the non-affine bubble deformation in turbulence at a relatively high void fraction. However, there are three bubbles (No. 6, 14, and 17) that have larger ϵ_V than others. For these three cases, bubbles suffer from the overlapping image problem in more than two cameras. Implementing VC does not improve much–ϵ_V is still at around 20%. This suggests that this method does not work well for data at a very high void fraction with many overlapping bubble images.

6. Experimental results

In our experiments, bubbles were released in turbulence and their deformation were recorded by all the six real cameras simultaneously. Fig. 9 shows two examples, (a) a weakly-deformed case that remains close to a sphere, and (b) a highly-deformed case that is about to break. To acquire bubble images at the highest contrast, the dynamics of both bubbles and their surrounding tracer particles were illuminated by LED panels from the back. Six LED panels were used to provide individual lighting for each camera.

The acquired images were uploaded to Maryland Advanced Research Computing Center to speed up the iterative process that this shape reconstruction algorithm requires. The outlines of bubbles were easily determined from the image contrast. The standard VH method was then employed to reconstruct the initial 3D geometries of all bubbles in the view. As shown in Fig. 9(a), even just with the VH method, the volume overestimation reduces by 21% when N_{cam} increases from 2 to 4 but only by 12% as N_{cam} increases from 4 to 6. For the highly deformed bubble, as shown in Fig. 9(b), the volume overestimation drops by 34% as N_{cam} increases from 2 to 4, showing a more significant improvement compared with the weakly-deformed case. Nevertheless, the benefit quickly declines to 12%, similar to the number for the weakly-deformed case. The results underscore the importance of having at least four real cameras for reconstructing complex geometries. Note that the reported percentage change is calculated by treating the six-real-camera reconstructed volume as the actual bubble volume. Since the six-real-camera reconstruction must still overestimate the actual volume, the percentage number should be larger than what was reported here.

After VH, the reconstructed shape of each bubble can be input into our VC method to continue refining the geometry. In Fig. 9, it is clear that the algorithm tends to over-correct the reconstructed bubble geometry for $N_{cam} = 2$ because very few constraint from two real cameras is present to stop the algorithm. In this case, the algorithm starts to smooth the actual tip of the elongated bubble. As N_{cam} becomes larger, VC performs really well for the weakly-deformed case, but the improvement is limited for the highly-deformed one. This suggests that the level of improvement is case sensitive, depending on many parameters, such as the aspect ratio, orientation, and concavity of the bubble geometry.

Once the shape is determined, the center of mass is obtained by averaging the 3D locations of all surface vertexes. The center of mass can then be tracked between frames to connect the 3D reconstructed shapes into a trajectory. Fig. 10 shows an example of such a trajectory with the reconstructed shape shown every 30 frames. The color of each geometry indicates the aspect ratio α. Note that the major and minor axes for a geometry that underwent the non-affine deformation do not have to be normal to each other. For our experiments, as every vertex of the entire surface is known, the ratio between the longest and the shortest vertex-center distances was used to quantify α.

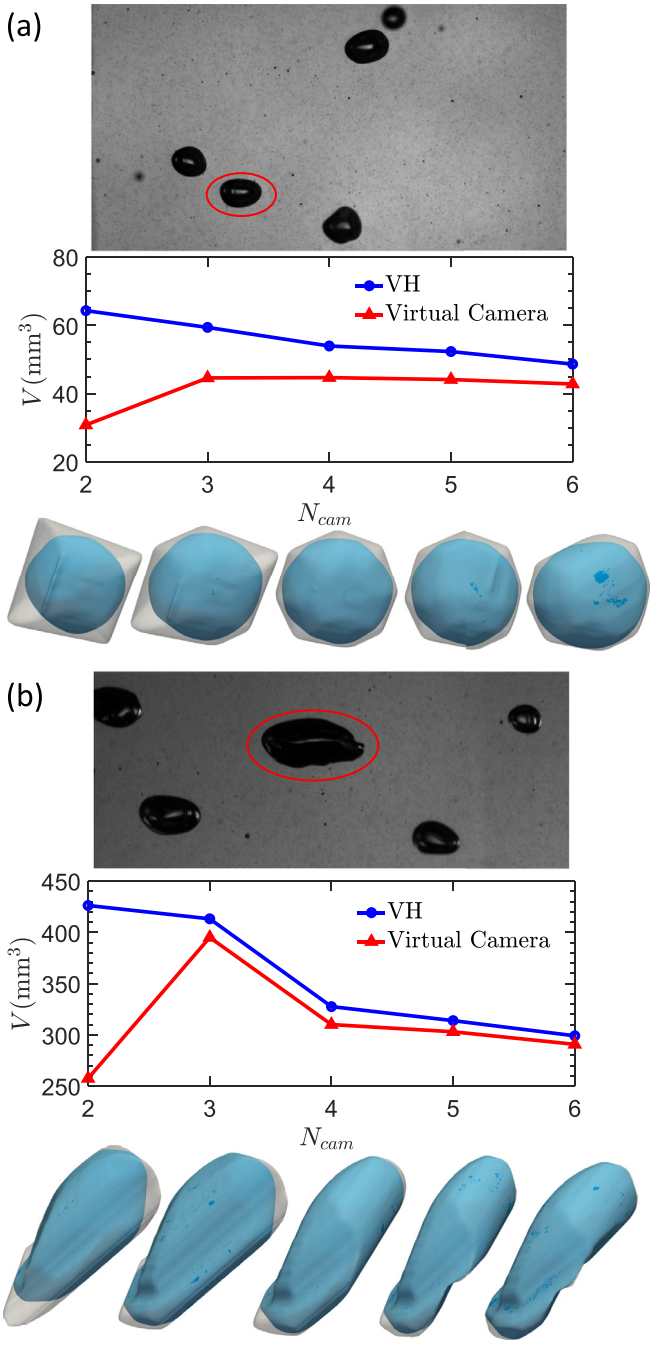

Fig. 9. A raw experimental image, the reconstructed volume V as a function of the number of real cameras N_{cam}, and the reconstructed 3D geometry (gray, VH; blue, Virtual Camera) of (a) a bubble that is close to sphere and (b) a bubble that has a large aspect ratio

The time trace of the bubble volume variation is shown in Fig. 11(a). This gas bubble did not merge with another one or break over the course of 0.5 s; Nor should it have significant mass transfer with the surrounding fluid, which implies that the observed large volume fluctuation may be an artifact due to the reconstruction uncertainty. In addition, the entire curve of the 3-real-camera configuration is systematically higher than that of the 6-real-camera case, which is consistent with what we expected that six cameras provide more constraints. But this difference is not very small, nearly 27%. In addition, there are four peaks from 0.2 s to 0.45 s, with the first peak slightly lower than the other three. For all four peaks, the image of this bubble overlaps with

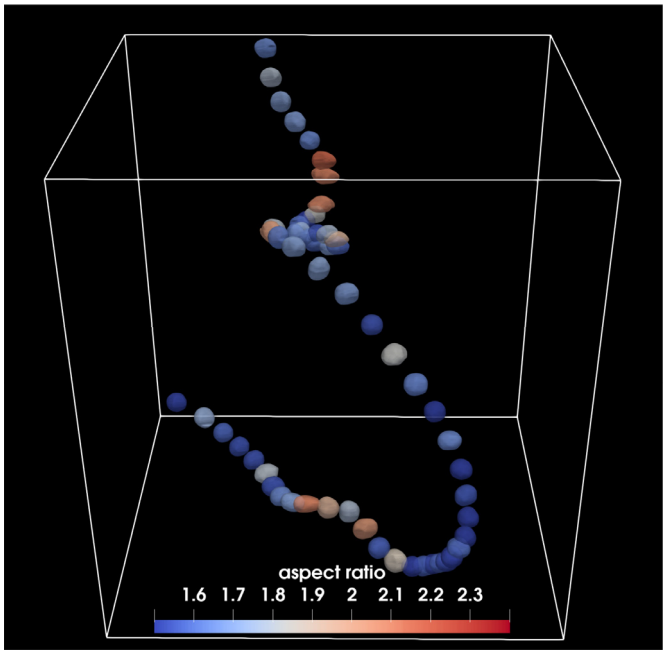

Fig. 10. The reconstructed bubble trajectory from an experimental dataset; only one every 30 frames is shown here. For each bubble, the surface is color-coded with the instantaneous bubble aspect ratio.

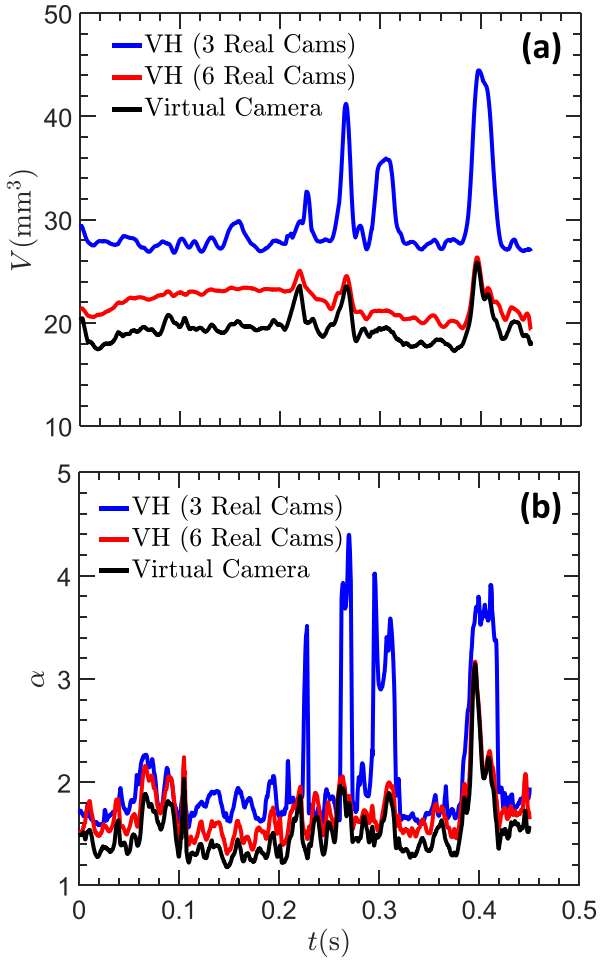

Fig. 11. Time trace of (a) the volume V and (b) the aspect ratio α of a trajectory as shown in Fig. 10. Three different lines show the reconstructed results using VH with 3 real cameras (blue), 6 real cameras (red), as well as 6 real cameras plus applying our VC method (black).

that of another one in at least one of the real cameras. The third peak falls back to normal as N_{cam} grows from 3 to 6 because two of three added cameras can clearly see the two bubbles as separate entities.

When the VC method is applied, it helps to remove more extra materials and brings the red curve systematically down by another 21% (the overall improvement from blue line to black line is 55%). In addition, it appears that the non-physical variation of the bubble volume in the red curve with the first 0.2 s systematically higher than the rest is gone after implementing the VC method. On the other hand, the improvement for the three peaks after implementing the VC method is small. As we mentioned before, this is inevitable as the geometrical constraint is lost in real cameras when the image of a bubble starts to overlap with that of another one nearby. Nevertheless, these events can be identified and removed during the post-processing step by relying on several key signatures: (i) the estimated volume is typically much larger than the mean of the trajectory, (ii) when the reconstructed 3D geometry is projected back onto 2D camera images, the projected area is much smaller than the detected area. Note that there is no solution to save these cases, the only thing that one can do is to remove them from the statistics. Segmenting images is often unreliable because two bubbles touching each other can be easily confused with a bubble that is close to breakup.

The time trace of the aspect ratio α for the same bubble is shown in Fig. 11(b). α exhibits many small fluctuations that are not seen in volume as taking the ratio between the major and minor axes amplifies noise. The systematical reduction of α from 3-real-camera with VH to 6-real-camera with VC is clear, and the benefit of increasing N_{cam} from 3 to 6 is also obvious as three major peaks that have abnormally-large $\alpha > 3.5$ are removed. Note that these four peaks correspond to the same four peaks in the time trace of the volume. This test case demonstrates the importance of not only having as many real cameras as one can afford but also using VC for complex deformable bubbles/droplets.

Finally, the reconstruction uncertainty of an experimental data needs to be assessed so we can be more selective in the post-processing step to calculate statistics. Since the actual volume of a bubble in an experimental dataset is not known, we cannot estimate ϵ_V as we did for synthetic datasets. However, we proposed another way to indirectly estimate ϵ_V based on the geometry and orientation for a given bubble. ϵ_V of a sphere, an ellipsoid, and a dumbbell for different orientations have been obtained in Section 4. Since they represent different states of bubble deformation, ϵ_V is plotted as a function of α from 1 to 9 (1 for sphere, 3 for ellipsoid, and 9 for dumbbell). Note that α is not well defined for a dumbbell since the minor axis of a dumbbell is close to zero and α is thus close to infinity. We decide to set its aspect ratio at 9, as there is a high probability for the neck to emerge and bubble to break at this aspect ratio.

For each frame, after the reconstruction, the direction of the major axis can be acquired and denoted as $\vec{a}$, from which the Euler angle can be determined. For the particular example used in Fig. 12(a) inset, the Euler angle is (154.6°, 42.1°, 0°). ϵ_V for three basic geometries at this specific Euler angle can be interpolated from the results shown in Figs. 6 and 7, and the results are shown as blue dots in Fig. 12. ϵ_V for the actual bubble at its $\alpha = 1.5$ (red dot) is estimated through a shape preserving piecewise cubic interpolation (blue line) from the three basic geometries.

The same calculation was repeated for all frames in one trajectory and the time trace of ϵ_V is acquired and shown in Fig. 12(b). The results show that the level of bubble volume overestimation for the first 0.2 s is probably higher than the rest. This is consistent with the result shown as the black curve in Fig. 11(a), in which the volume of the reconstructed geometry is indeed slightly higher in the first 0.2 s. Nevertheless, this uncertainty

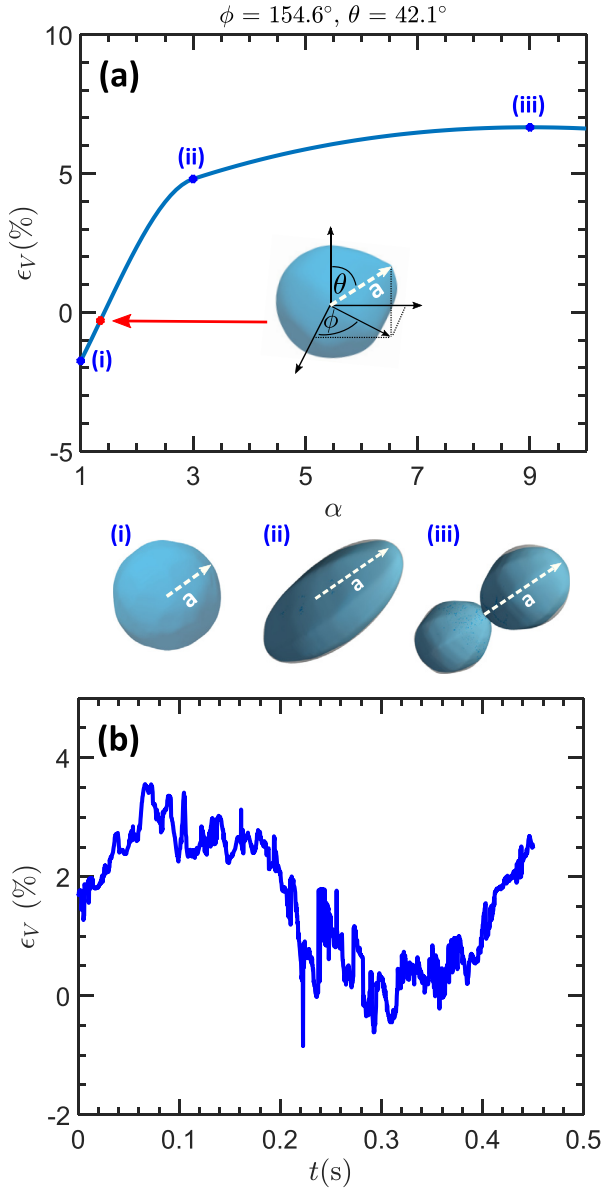

Fig. 12. (a) The uncertainty of volume reconstruction ϵ_V versus aspect ratio α for three cases: (i) sphere ($\alpha = 1$), (ii) ellipsoid ($\alpha = 3$), (iii) dumbbell ($\alpha = 9$). The inset shows the reconstructed geometry of an actual bubble with $\alpha = 1.5$ and Euler angles at (154.6°, 42.1°, 0°). ϵ_V of such a reconstruction is shown as the red dot by interpolation. (b) the estimated ϵ_V of the entire trajectory.

quantification did not capture those large peaks in the volume estimation because this method only takes the geometry and orientation into account without knowing the presence of overlapping bubble images.

7. Conclusion and remarks

This paper introduces a new virtual-camera method to improve the reconstruction accuracy for bubbles or droplets undergoing non-affine deformation in turbulence. This new method translates the physical constraint of the minimal surface curvature to the image refinement on virtual cameras. The extra materials due to the limited-angle reconstruction manifest as sharp corners on the virtual-camera planes, which can be smoothed and removed. The algorithm was first tested on three simple synthetic objects, including sphere, ellipsoid, and dumbbell. They represent three basic states of bubble deformation: undeformed, weakly-deformed, and severely-deformed. The reconstruction uncertainty appears to depend on both the bubble geometry (convex or concave) and its orientation with respect to the camera configuration. Our method works well for simple and convex geometries using as few as two real cameras. More real cameras are required for either complex shapes or geometries with concave features. In addition to these simple geometries, a DNS dataset of bubble undergoing non-affine deformation in turbulent channel flow is used to quantify the uncertainty, and it turns out that the VC method reduces the volume overestimation from 20% to 10%. Finally, the reconstruction has also been tested on the experimental data of the non-affine bubble deformation in strong turbulence. The volume overestimation drops from about 55% using 3 real cameras with the classical VH method to about 4% using 6 real cameras and the VC method. In addition, the method also utilizes the estimated geometrical aspect ratio and orientation to assess the reconstruction uncertainty of each bubble in each frame, which can be leveraged to select the best reconstruction for statistics. In summary, this method provides a robust way to incorporate the physical constraints to improve the 3D reconstruction accuracy of bubbles and droplets in turbulent multiphase flow and it also paves the foundation for the future development of uncertainty quantification for strongly coupled gas-liquid and liquid-liquid multiphase flow.

Acknowledgement

Acknowledgment is made to the Donors of the American Chemical Society Petroleum Research Fund for partial support of this research. This material is also based upon work supported by the National Science Foundation under Grant No. 1705246 and CAREER-1653389. The authors also want to thank Gretar Tryggvason and Jiacai Lu for sharing the DNS dataset.

Supplementary material

Supplementary material associated with this article can be found, in the online version, at doi:10.1016/j.ijmultiphaseflow.2019.103088.

References

Adhikari, D., Longmire, E., 2012. Visual hull method for tomographic PIV measurement of flow around moving objects. Exp. Fluids 53, 943–964.
Besagni, G., Inzoli, F., 2016. Bubble size distributions and shapes in annular gap bubble column. Exp. Ther. Fluid Sci. 74, 27–48.
Fu, Y., Liu, Y., 2016. Development of a robust image processing technique for bubbly flow measurement in a narrow rectangular channel. Int. J. Multiph. Flow 84, 217–228.
Fu, Y., Liu, Y., 2018. 3D bubble reconstruction using multiple cameras and space carving method. Measur. Sci. Technol. 29, 075206.
Fujiwara, A., Danmoto, Y., Hishida, K., Maeda, M., 2004. Bubble deformation and flow structure measured by double shadow images and PIV/LIF. Exp. Fluids 36, 157–165.
Furukawa, Y., Ponce, J., 2009. Carved visual hulls for image-based modeling. Int. J. Comput Vis. 81, 53–67.
Galindo, E., Pacek, A.W., Nienow, A.W., 2000. Study of drop and bubble sizes in a simulated mycelial fermentation broth of up to four phases. Biotechnol. Bioeng. 69, 213–221.
Giovannettone, J., Tsai, E., Gulliver, J.S., 2009. Gas void ratio and bubble diameter inside a deep airlift reactor. Chem. Eng. J. 149, 301–310.
Honkanen, M., 2009. Reconstruction of three-dimensional bubble surface from high-speed orthogonal imaging of dilute bubbly flow. In: Proceedings of the Computational Methods in Multiphase flow V, New Forest, UK, pp. 469–480.
Isidoro, J., Sclaroff, S., 2003. Stochastic refinement of the visual hull to satisfy photometric and silhouette consistency constraints. In: Proceedings of the ICCV, p. 1335.
Jordt, A., Zelenka, C., von Deimling, J.S., Koch, R., Köser, K., 2015. The bubble box: towards an automated visual sensor for 3d analysis and characterization of marine gas release sites. Sensors 15, 30716–30735.
Kanatani, K.i., Chou, T.C., 1989. Shape from texture: general principle. Artif. Intell. 38, 1–48.
Kutulakos, K.N., Seitz, S.M., 2000. A theory of shape by space carving. Int. J. Comput. Vis. 38, 199–218.

Laurentini, A., 1994. The visual hull concept for silhouette-based image understanding. IEEE Trans. Pattern Anal. Mach. Intell. 16, 150–162.
Lu, J., Tryggvason, G., 2008. Effect of bubble deformability in turbulent bubbly upflow in a vertical channel. Phys. Fluids 20, 040701.
Maldonado, M., Quinn, J., Gomez, C., Finch, J., 2013. An experimental study examining the relationship between bubble shape and rise velocity. Chem. Eng. Sci. 98, 7–11.
Matusik, W., Buehler, C., Raskar, R., Gortler, S.J., McMillan, L., 2000. Image-Based Visual Hulls. ACM Press/Addison-Wesley Publishing Co.
Medoff, B.P., Brody, W.R., Nassi, M., Macovski, A., 1983. Iterative convolution backprojection algorithms for image reconstruction from limited data. JOSA 73, 1493–1500.
Mulayim, A.Y., Yilmaz, U., Atalay, V., 2003. Silhouette-based 3-d model reconstruction from multiple images. IEEE Trans. Syst. Man Cybern. Part B Cybern. 33, 582–591.
Ni, R., Huang, S.D., Xia, K.Q., 2012. Lagrangian acceleration measurements in convective thermal turbulence. J. Fluid Mech. 692, 395–419.
Ouellette, N.T., Xu, H., Bodenschatz, E., 2006. A quantitative study of three-dimensional lagrangian particle tracking algorithms. Exp. Fluids 40, 301–313.
Rau, M.J., Vlachos, P.P., Garimella, S.V., 2016. A tomographic-PIV investigation of vapor-induced flow structures in confined jet impingement boiling. Int. J. Multiph. Flow 84, 86–97.
Ravelet, F., Colin, C., Risso, F., 2011. On the dynamics and breakup of a bubble rising in a turbulent flow. Phys. Fluids 23, 103301.
Ristroph, L., Berman, G.J., Bergou, A.J., Wang, Z.J., Cohen, I., 2009. Automated hull reconstruction motion tracking (HRMT) applied to sideways maneuvers of free-flying insects. J. Exp. Biol. 212, 1324–1335.
Sidky, E.Y., Kao, C.M., Pan, X., 2006. Accurate image reconstruction from few-views and limited-angle data in divergent-beam CT. J. X-ray Sci. Technol. 14, 119–139.
Sidky, E.Y., Pan, X., 2008. Image reconstruction in circular cone-beam computed tomography by constrained, total-variation minimization. Phys. Med. Biol. 53, 4777.
Sun, X., Smith, T.R., Kim, S., Ishii, M., Uhle, J., 2002. Interfacial area of bubbly flow in a relatively large diameter pipe. Exp. Therm. Fluid Sci. 27, 97–109.
Tan, S., Salibindla, A., Masuk, A.U.M., Ni, R., 2019. An open-source shake-the-box method and its performance evaluation. In: Proceedings of the 13th International Symposium on Particle Image Velocimetry.
Tsai, R.Y., 1986. An efficient and accurate camera calibration technique for 3d machine vision. In: Proceedings of the Computer Vision and Pattern Recognition, pp. 364–374.
White, B., 1982. Two-phase measurements of saltating turbulent boundary layer flow. Int. J. Multiph. Flow 8, 459–473.
Wieneke, B., 2008. Volume self-calibration for 3d particle image velocimetry. Exp. Fluids 45, 549–556.
Woolf, D.K., 1997. Bubbles and their role in gas exchange. The Sea Surface and Global Change.